Accepted manuscript (author version)

To appear in:

Iranian Journal of Earth Sciences (Iran J. Earth. Sci.)

E-ISSN: 2228-785X Print ISSN: 2008-8779

Received: 11 July 2025

Revised: 29 September 2025

Accepted: 13 October 2025

DOI: https://doi.org/10.57647/ijes.2026.18286

Original Research

Ore-forming Fluid Evolution in the Shourab Gold Prospect, Isfahan: Insights from Quartz Chemistry and Fluid Inclusions

Alireza Rezaei Alishahdani[1], Alireza Jafarirad[*1], Zahra Alaminia[*2], Mehran Arian[1], Hemayat Jamali[3], Manuel Nopeia[4,5], Renaldi Suhendra[6]

[1] Department of Earth Sciences, SR.C., Islamic Azad University, Tehran, Iran

[2] Department of Geology, Faculty of Science, Ferdowsi University of Mashhad, Mashhad, Iran

[3] Department of Geology, University of Isfahan, Isfahan, Iran

[4] Future Cooperative Research Organization, Akita University, Akita, Japan

[5] Department of Geology, Faculty of Science, University of Johannesburg, Auckland Park, South Africa

[6] Research Center for Geological Resources, National Research, and Innovation Agency (BRIN), Indonesia

* Corresponding authors: alireza_jafarirad@iau.ac.ir , alaminia@um.ac.ir

Abstract

This study investigates the ore-forming fluid evolution in the Shourab gold prospect, Central Iran, through integrated quartz chemistry and fluid inclusion analysis. The Shourab gold prospect occurs within the early Eocene diorite to granodiorite, intruding the Cretaceous carbonate and volcanic rocks. The prospect displays alteration zone of sodic-calcic, biotite-magnetite, carbonatization, and silicification associated with gold mineralization. Early-stage quartz from biotite-magnetite alteration zone contains elevated Ti (BDL-410 ppm), formed from high-temperature (T_h of fluid inclusions= 343–495 °C, mode= 390 °C) and saline (11–29 wt% NaCl eq., avr. 17 wt% NaCl eq.). Late-stage quartz in silicified zones shows significant Al (704–2307 ppm) and alkali enrichment (BDL–349 ppm Na and 96–247 ppm K), associated with cooler (198–338 °C, mode= 324 °C), less saline fluids (7–11 wt% NaCl eq., avr. 8 wt% NaCl eq.). Gold mineralization is associated with late-stage fluids, where cooling of hydrothermal fluids promoted metal deposition. Veins formed by low-temperature, less saline fluids with high Al and alkali elements in quartz serve as a potential for Au mineralization and can guide future exploration in the region.

Keywords: Central Iran, Shourab, Quartz chemistry, Fluid inclusions, Gold mineralization.

1. Introduction

The Shourab gold prospect is located 8 km southeast of the active Kuh-e Dom gold mine of Isfahan province, Iran, with 1 Mt Au resource at 1.05 g/t average grade (Mehrabi et al., 2014; Tale Fazel, 2014; Tale Fazel et al., 2015; Farangi et al., 2023; Fig. 1a). Previous studies classified the Shourab gold prospect as an iron oxide copper gold (IOCG)-type, similar to the nearby Kuh-e Dom ore deposit (Tale Fazel et al., 2015), based on the remote sensing analysis of iron assemblages and alteration patterns (Farangi et al., 2021). Recent investigations of bulk geochemistry of Shourab intrusions further support this IOCG classification (Farangi et al., 2023). However, the porphyry-Cu affinity was also proposed by Sarjoughian et al. (2015a) based on biotite chemistry from the Kuh-e Dom.

Quartz is the predominant gangue mineral in the Shourab gold prospect, which occurs in nearly all mineralization stages. Quartz serves as a valuable indicator of magmatic-hydrothermal processes due to its chemical stability and resistance to alteration (Larsen et al., 2000; 2004). High-purity quartz typically contains trace elements at concentrations <100 ppm (Al<30 ppm, Ti<10 ppm, Na and K<8 ppm, Fe<3 ppm; Dennen, 1966; Rusk and Reed, 2002; Rusk et al., 2008; Müller et al., 2010; 2012; Rusk et al., 2011; Rusk, 2012), with lattice substitutions controlled by temperature, fluid chemistry, pH, and oxygen fugacity (Götze, 2009, 2012, 2021; Elmi et al., 2025). These chemical characteristics provide an invaluable petrogenetic indicator for reconstructing ore-forming conditions (Wertich et al., 2018; Dabiri et al., 2018; Manalo et al., 2020; Rottier and Casanova, 2021; Mollai et al., 2021; Gao et al., 2022; Mazandarani et al., In press), especially when it is combined with fluid inclusion analysis (Zhou et al., 2023). The growing body of research on trace element compositions of quartz from a wide range of mineralizing systems (e.g., porphyry, epithermal, Mississippi Valley Type) has highlighted systematic variations that can be used as exploration tools, providing new insights into the genetic processes and ore potential of different deposits (Mao et al., 2017; Rottier and Casanova, 2021; Talebian Borojenie et al., 2025). This study integrates quartz chemistry and fluid inclusion microthermometry analyses to reconstruct the magmatic-hydrothermal evolution of gold mineralization at Shourab. We focus on understanding the hydrothermal processes, including temperature and source of fluids, as well as mechanism of gold precipitation.

2. Geological Background

The Shourab gold prospect is situated near the Kuh-e Dom massif on the western margin of Central Iran, approximately 85 km east of the Urumieh-Dokhtar Magmatic Arc (UDMA) (Fig.1a). Fazel (2014) suggests the Kuh-e Dom massif is an isolated remnant arc, separated from the main body of the UDMA. UDMA has been active during the Mesozoic and Cenozoic, driven by prolonged Neotethyan subduction and subsequent continent–continent collision (Chiu et al., 2013; Babazadeh et al., 2019).

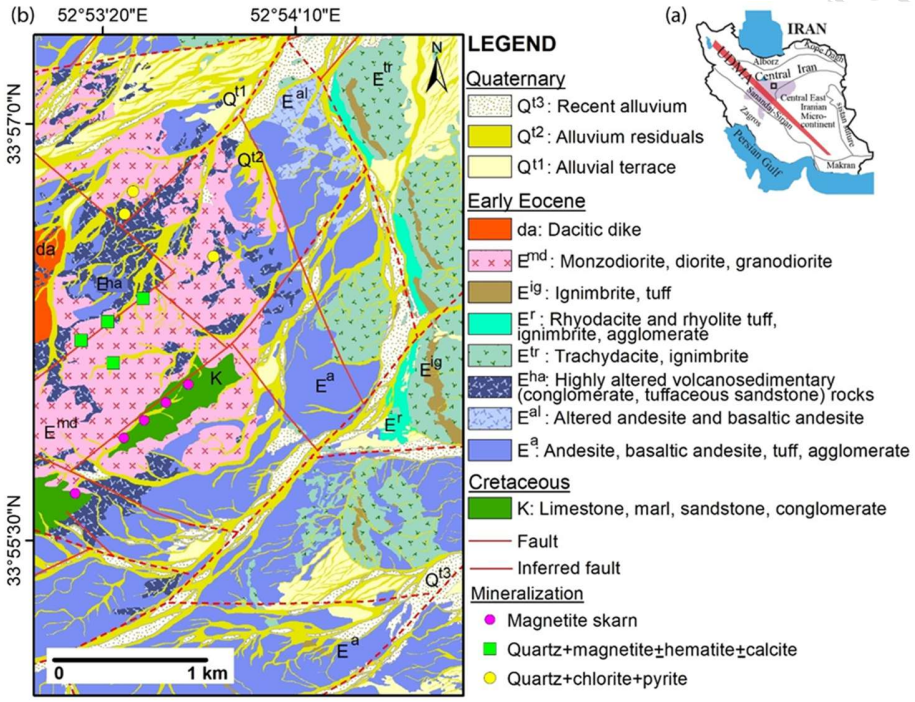

Figure 1. (a) The map shows the location of the Shourab gold prospect in relation to the Urumieh-Dokhtar Magmatic Arc (UDMA) in Central Iran, as well as its position in Isfahan Province (violet color). (b) Geological map of the Shourab area, highlighting the dacitic dikes (western sector) as the youngest exposed magmatic unit in the region.

The basement of Shourab comprises of the Kuh-e Dom metamorphic complex, which includes greenschists, phyllites, and subordinate crinoid-bearing limestone and sandstone, with ages ranging from 333 to 320 Ma (Romanko et al., 1984; Bagheri and Stampfli, 2008, Haschke et al., 2010). This unit is unconformably overlain by thin- to medium-bedded Cretaceous crystalline limestone, with basal conglomerate and cream to brown marl interlayers (Fig. 2a). In the Shourab area, the sequence trends are NE-SW and is covered by Eocene igneous units**.** Fossil assemblages

(e.g., Orbitolina and echinoderms) confirm a lower Cretaceous age for limestone (Figs. 2a). Cenozoic igneous rocks, coeval with intrusions, consist of volcanic, volcaniclastic, and clastic rocks, occasionally interbedded with carbonate layers. These are locally overlain by late Eocene volcanic rocks, widely exposed across the study area. The volcanic suite ranges from calc-alkaline to shoshonitic (felsic to intermediate) in compositions, which includes rhyolite, rhyodacite, dacite, acidic tuff, ignimbrite (Fig. 2b), andesite, and basaltic andesite (Shahzeydi et al., 2008, Kananian et al., 2011; 2014; Sarjoughian et al., 2012; 2014). The Eocene sedimentary sequence features conglomerate, tuffaceous sandstone, and nummulitic limestone (Fig. 1b). Chemical data suggest shoshonitic magmatism occurred during the transition from primitive to a mature continental margin arc (Farangi et al., 2023). Intrusive bodies are dominated by gabbro, diorite, quartz diorite, monzodiorite, monzonite, granodiorite, and minor granite (Fig. 1b). In most of these intrusive bodies, amphibole has undergone carbonatization, wheres primary biotite crystals have remained largely unaltered. Sarjoughian et al. (2015b) reported the U-Pb zircon age of 51.1± 0.4 Ma, determined from 24-point U-Pb analysis. However, they noted that mafic-intermediate rocks yielded an older age (53.9±0.4 Ma) compared to felsic ones. In contrast, Sharkovski et al. (1981) proposed a younger K-Ar amphibole age for the intrusions (40.2±2.2 and 35.5±1.1 Ma). These magmatic rocks are genetically associated with the iron, copper, and gold mineralization, as observed at Kuh-e Dom and Shourab (Tale Fazel et al., 2015; Farangi et al., 2023). The volcanic and intrusive rocks are crosscut by subvolcanic dacite (light-colored, extending up to 800 m in length; Figs. 1b, 2b). The entire sequence is unconformably overlain by Quaternary sediments (Fig. 1b).

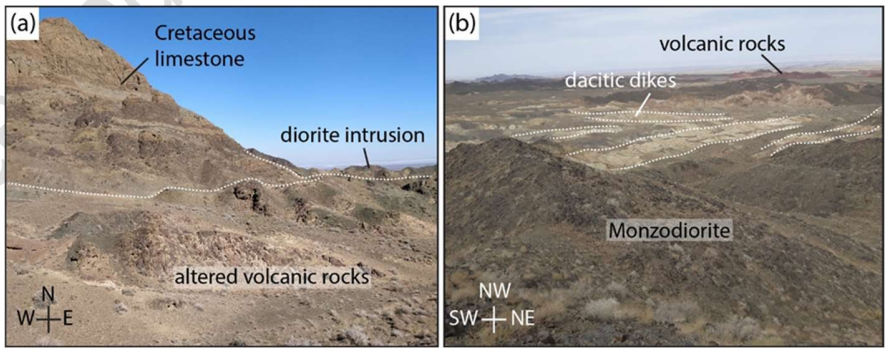

Figure 2. Field photographs from the Shourab gold prospect. (a) Outcrop exposure showing crystallized limestone, volcanic, and intrusive rocks in the study area. (b) Panoramic view demonstrating the relationship between light-colored dacitic dikes and monzodiorite intrusion.

3. Materials and Methods

A total of 43 samples were collected from outcrops and drill cores of Shourab gold prospect, and petrographic observations were conducted to describe the mode of occurrence and texture of quartz and carbonate within the alteration zones.

Electron probe micro analysis (EPMA) was performed using a JEOL JXA 8230. The EPMA was carried out at the Akita University, Japan. Quartz and carbonate were analyzed with a 5 μm beam size, under an acceleration voltage of 15 kV and a beam current of 20 nA (Tables 1 and 2). The following set of natural and synthetic standards were used for the analysis: quartz for Si, jadeite for Na, hematite for Fe, wollastonite for Ca, K-feldspar for K, pyrophanite for Ti and Mn, eskolaite for Cr, corundum for Al, and enstatite for Mg. The peak background time was set at 20/10 s for Si, Al, K, Ca, Mg, Mn, Fe, and Ti, and 40/20 s for Cr. Despite the lower peak/background measuring time applied, the average limit of detections was optimized to 141, 134, 216, 217, 189, 142, 147, 148, 44, and 49 ppm for Na, Mg, Al, Cr, Mn, Ti, Fe, Si, K, and Ca, respectively.

Seven doubly polished thin sections (0.2-0.3 mm thick) were prepared from quartz and carbonate samples for fluid inclusion studies, representing alteration zones (biotite-magnetite alteration, carbonatization, and silicification). Microthermometric analyses were measured using a Linkam THMS G-600 heating-freezing stage (operational range: –180 to +600 °C). Fluid inclusions of ore-bearing quartz and carbonate were analyzed following the methods outlined of Roedder (1984). Salinity (wt.% NaCl eq.) were calculated using parameters such as final ice melting temperature (Tm_{ice}) and homogenization temperatures (T_h) in the MacFlinCor software (Brown and hagemann, 1994, 1995) (Table 3). Sample preparation was conducted at the Zarazma Lab, while fluid inclusion micothermomatry was conducted at the Fluid Inclusion Laboratory of Iranian Mines and Mining Industries Development and Renovation (IMIDRO).

4. Hydrothermal Alteration and Ore Mineralization

Gold mineralization is mainly hosted by intrusive rocks, with subordinate volcanic sequences. Hydrothermal alteration overprints both volcanic (andesite to rhyolite) and intrusive rocks, particularly in the northern and southern parts of the prospect area. Alteration intensity varies from weak to moderate (35 to 60%) in host rocks and can be classified into different stages: (1) pre-ore stage: characterized by sodic-calcic alteration, represented by albite, tremolite-actinolite, and

tourmaline (Fig. 3d); (2) early-ore stage: dominated by biotite-magnetite alteration featuring biotite, K-feldspar, magnetite, and quartz minerals (Fig. 3a, e); (3) transition-stage: marked by carbonatization with carbonate, and minor pyrite ± chalcopyrite; (4) late-ore stage: defined by silicification, consisting of quartz, sericite, pyrite, chalcopyrite assemblages; and (5) post-ore stage: comprise of chlorite alteration, represented by chlorite, calcite, quartz, epidote, and hematite. Among these, stages 3 and 5 are widely developed in the study area and are particularly well expressed in the Shourab gold prospect (Fig. 3c). The gold concentrations observed in the whole-rock analyses are primarily associated with alteration stages 3 and 4, indicating that gold mineralization is closely linked to the transition and late-ore stages.

Three types of ore are recognized in the Shourab gold prospect, i.e., Fe oxide ore, sulfide ore, and mixed Fe oxide-sulfide ores (Fig. 3a, f). These ores occur in massive, disseminated, banded, vein-veinlet, and brecciated forms. Magnetite typically forms disseminated grains, massive replacements, nodular aggregates, breccia (Fig. 3b), and banded magnetite layers within mafic-intermediate rocks (Farangi et al., 2023). Hematite- quartz assemblages occur as veinlets and open-space filling associated with felsic intrusions (Fig. 3c). Sulfide mineralization consists of fracture-coating pyrite with rare chalcopyrite or sphalerite in quartz veins (Fig. 3g). Gold occurs predominantly in quartz-sulfide veins and fracture-controlled altered zones, associated with silicification and carbonatization. Whole rock analyses of quartz vein indicated gold contents ranging from 6 to 104 ppb, whereas EPMA data reveal up 58.9 ppb Au within pyrite. Native gold has not been identified in the area; instead, pyrite and chalcopyrite constitute the main sulfide minerals and the principal carrier of gold, occurring within vein and veinlets (Fig. 3f). Although gold grades are frequently recorded, no economically significant concentrations have been measured to date.

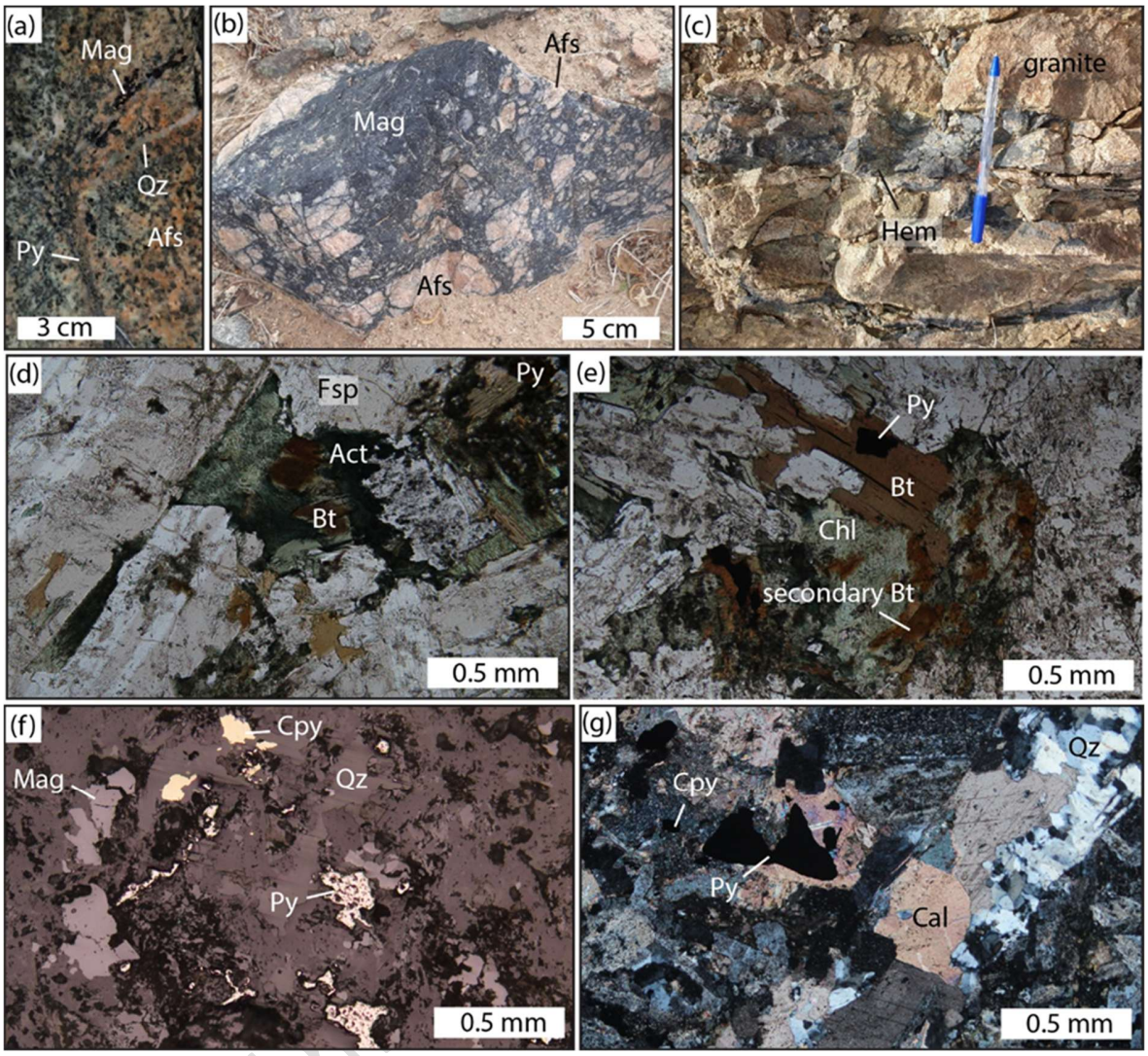

Figure 3. Field photographs, hand specimen photos, and photomicrographs from the Shourab gold prospect. (a) Potassic-altered rock crosscut by quartz-pyrite veinlets, locally overprinted by chlorite (sample $SH_7B_9S_{38}$). (b) Angular brecciated fragments of altered country rock cemented by magnetite. (c) Quartz-hematite vein with a chlorite alteration halo in the granite wall rock. (d) Primary biotite partially replaced by actinolite/tremolite. (e) Secondary biotite and magnetite associated with potassic alteration. (f) Pyrite and chalcopyrite with quartz, replacing feldspar in quartz diorite. (g) Pyrite- quartz vein formed after carbonatization; note to fine-grained crystals along the the veinlet margins. Photomicrographs taken in transmitted light (d, f), cross polarized light (g), and reflected light (f). Mineral abbreviation according to Warr (2021): Act-actinolite, Afs-alkali feldspar, Cal-calcite, Ccp-chalcopyrite, Chl-chlorite, Fsp-feldspar, Hem-hematite, Mag-magnetite, Py-pyrite, Qz-quartz.

5. Results

5.1. Quartz Chemistry

The results of EPMA data from the Shourab gold prospect reveal distinct compositional variations between early- and late-stage quartz (Table 1). Early-stage quartz, associated with biotite-magnetite alteration, exhibits elevated Ti (BDL–410 ppm) and depleted alkali element concentrations (BDL–505 ppm Al and BDL–81 ppm K). In contrast, late-stage quartz from silicified zone shows significant enrichment in Al (704–2307 ppm), Na (BDL–349 ppm), K (96–247 ppm), and depleted in Ti concentrations (BDL) (Table 1).

Table 1. Minor and trace element composition of early- and late-quartz determined from the Shourab gold prospect. The results for all elements (ppm) were calculated from oxide values (wt%), except for SiO_2, which is presented in wt.% directly from EPMA analyses.

Quartz type	Point No.	Al (ppm)	Ti (ppm)	K (ppm)	Fe (ppm)	Na (ppm)	Mn (ppm)	Ca (ppm)	SiO_2 (%)
Detection		216	142	44	147	141	189	49	0.148
Qz-Mag	SQ1-1	BDL	BDL	BDL	875	BDL	BDL	BDL	100.36
Qz-Mag	SQ1-2	BDL	BDL	BDL	163	BDL	BDL	63	100.23
Qz-Mag	SQ1-3	311	BDL	BDL	448	BDL	BDL	BDL	99.96
Qz-Mag	SQ1-4	BDL	410	48.8	215	BDL	BDL	91	100.52
Qz-Mag	SQ1-5	259	BDL	BDL	108	BDL	BDL	BDL	100.75
Qz-Mag	SQ1-6	505	BDL	80.5	892	BDL	BDL	222	100.57
Qz-Mag	SQ1-7	451	BDL	BDL	985	BDL	BDL	69	100.09
Qz-Py	SQ2-1	704	BDL	114	2879	349	BDL	476	99.94
Qz-Py	SQ2-2	2307	BDL	247	1182	BDL	BDL	BDL	99.13
Qz-Py	SQ2-3	1161	BDL	106	1422	208	BDL	BDL	99.10
Qz-Py	SQ2-4	1683	BDL	95.8	1371	245	BDL	229	99.07

Notes: BDL= below the detection limit,

5.2. Carbonate minerals Chemistry

EPMA data of carbonate minerals from carbonatization alteration zone in the Shourab gold prospect indicate a predominantly calcite composition, characterized by MnO (0.39–2.89wt%), FeO (0.46–1.74 wt%), and low MgO (0.06–0.80 wt%) and TiO_2 (BDL–0.04 wt%) contents, with Na_2O below detection limits (Fig. 4; Table 2).

Table 2. Chemical composition of calcite from the Shourab gold prospect.

Point	Na_2O	MgO	Al_2O_3	Cr_2O_3	TiO_2	FeO	MnO	SiO_2	CaO	K_2O	Total
SC-1	BDL	0.36	0.09	BDL	0.04	1.61	2.89	0.30	53.92	0.06	59.27
SC-2	BDL	0.81	0.61	BDL	0.01	1.74	1.20	1.02	54.45	0.03	59.87
SC-3	BDL	0.12	0.01	BDL	BDL	0.46	0.62	BDL	53.93	0.02	55.16
SC-4	BDL	0.17	BDL	BDL	0.00	1.49	0.39	0.04	54.17	0.02	56.28
SC-5	BDL	0.06	0.01	BDL	0.01	0.39	1.79	0.01	54.21	0.00	56.48
SC-6	0.030	0.15	0.13	BDL	0.01	0.62	1.88	0.04	53.98	0.04	56.88

Note: BDL= below the detection limit,

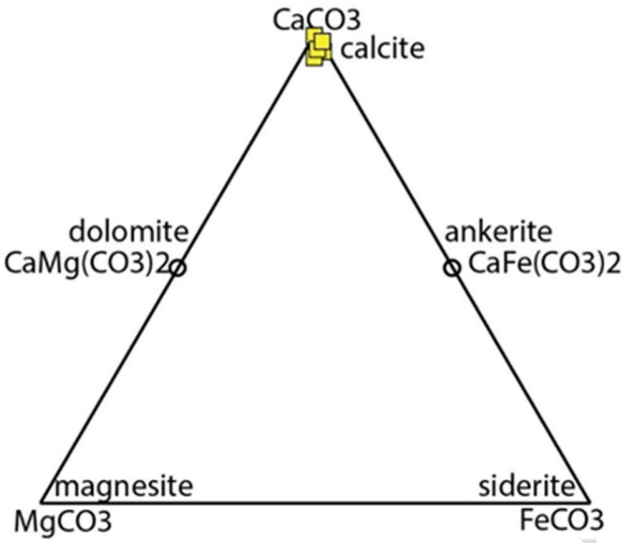

Figure 4. Chemical classification of carbonate minerals from the Shourab gold prospect.

5.3. Fluid inclusion

5.3.1. Petrography

Fluid inclusion studies were conducted on quartz from biotite-magnetite alteration and silicification zones, and calcite from the carbonatization zone at the Shourab gold prospect. Calcite crystals typically contain fewer inclusions than quartz. The studied inclusions in both minerals are predominantly primary and liquid-rich (Fig. 5a-e). They exhibit sizes of 5–30 μm and diverse morphologies including regular, rounded, elongated, trigonal, and negative crystal shapes. Petrographic analysis identified three inclusion types: (I) rare single-phase (V- or L-type) inclusions (<5 μm in size, Qz-Mag stage), where liquid-dominated types form elliptical clusters in quartz; (II) abundant two-phase (LV-type) inclusions containing liquid + vapor (15–60 vol% vapor) that homogenize to liquid (T_h LV→L), observed in both minerals (Fig. 5a–c), with trace CO_2. Densely clustered gas-liquid inclusions (2–5 μm in size, Qz-Py stage) show elliptical, subrounded, or oblong morphologies; and (III) rare three-phase (LVS-type) and polyphase (LVS_1S_2-type) inclusions (8–30 μm in size, Qz-Mag stage) in the early quartz, with cubic halite, rounded corners sylvite, and opaque daughter minerals (Fig. 5d, e).

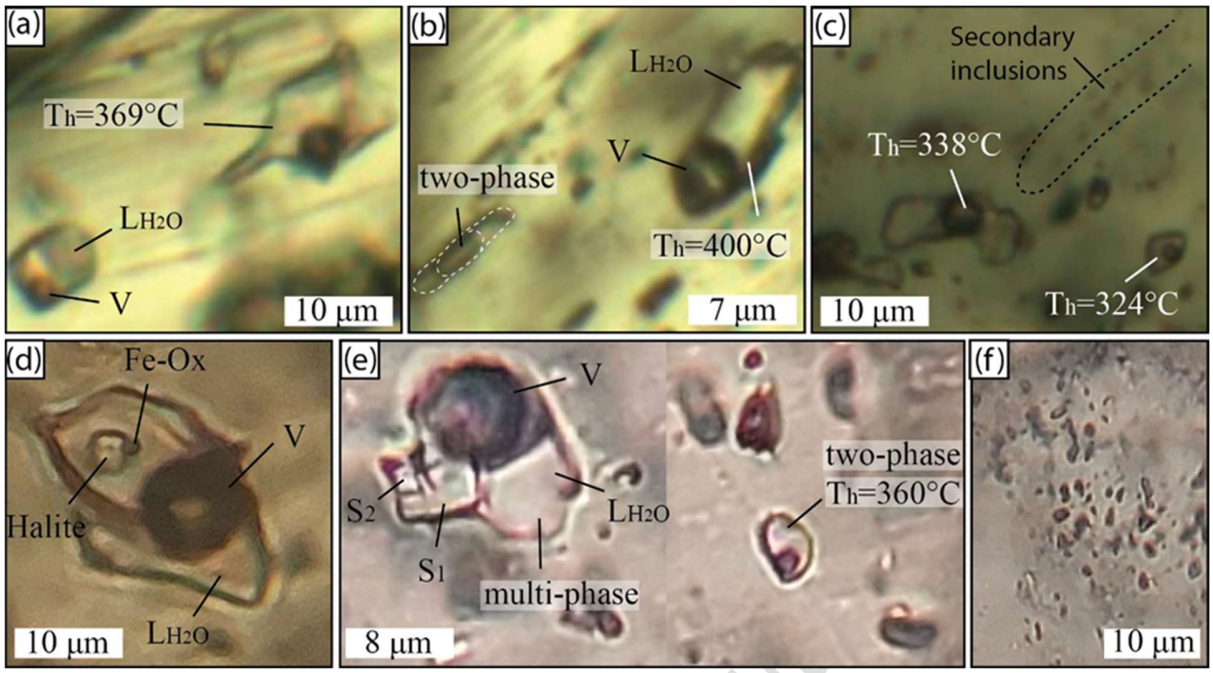

Figure 5. Photomicrographs of representative fluid inclusions observed in quartz and calcite from Shourab gold prospect. (a) Primary liquid-rich (LV-type) aqueous inclusion in quartz from the quartz-magnetite assemblage from the biotite- magnetite alteration zone (sample $SH_2B_{25}S_{124}$). (b) Type II (LV-type) inclusion in quartz from the quartz-magnetite assemblage (sample $SH_7B_8S_{34}$), (c) Type II (LV-type) inclusion in quartz from the quartz-pyrite assemblage of the silicification zone (sample $SH_5B_{18}S_{85}$). (d) Type III (LVS-type) inclusion in quartz from the biotite-magnetite alteration zone, showing halite and an opaque daughter mineral (sample $SH_2B_{26}S_{131}$). (e-f) Coexisting Type II (LV-type) and III (LVS_1S_2-type) inclusion in quartz from Fe-K alteration zone with trace CO_2 (sample $SH_4B_{31}S_{306}$). Note cubic halite and smaller sylvite crystals with slightly rounded corners. Abbreviations: L-liquid, V-vapor, S-halite, S_1S_2-halite/sylvite.

5.3.2. Microthermometry

Microthermometry analysis was performed on the LV and some LVS inclusions (Table 3). In the biotite-magnetite alteration zone (early mineralization, ore stage-I), quartz-associated magnetite contains mainly LV-type and rare LVS_1S_2-type and V-type inclusions (Fig. 5a, b, d, e, f). LV inclusions show first melting temperatures at –26.0 to –21.9 °C suggesting Na^+-K^+-rich fluids, Tm_{ice} values of -15.5 to -7.5 °C (salinities: 11.10–19.05 wt% NaCl eq.), and T_h values of 343–495 °C (Fig. 6). One halite-bearing inclusion homogenized by vapor disappereance at 384 °C, with a halite dissolution temperature (Tm_{NaCl}) of 214 °C, corresponding to a salinity of 28.58 wt% NaCl equivalent (Table 3). Variable fluid inclusion vapor/liquid ratios suggest heterogeneous trapping

during fluid boiling (sample $SH_4B_{31}S_{306}$, Figs. 6, 7). Early-stage quartz (ore stage-I), inferred to have formed at depths of 0.6–2.5 km, assuming a lithostatic pressure conditions (150–600 bar; Hezarkhani and Williams-Jones, 1998; Fig. 7), exhibits variable homogenization temperatures attributable to boiling under decreasing hydrostatic pressure. In the carbonatization zone (stage II), calcite hosts LV-type inclusions (Fig. 6), with T_h = 278–353°C and Tm_{ice} = -8.90 to -7.60 °C (salinities: 11.22–12.73 wt% NaCl eq.). In the late-ore stage silicification zone (ore stage III), quartz contains LV-type inclusions. LV inclusions record the lowest T_h (198–338 °C) and salinities (Tm_{ice}: -7.5 to -4.2 °C; 6.74–11.10 wt% NaCl eq.), reflecting significant cooling of the hydrothermal system (Fig. 7).

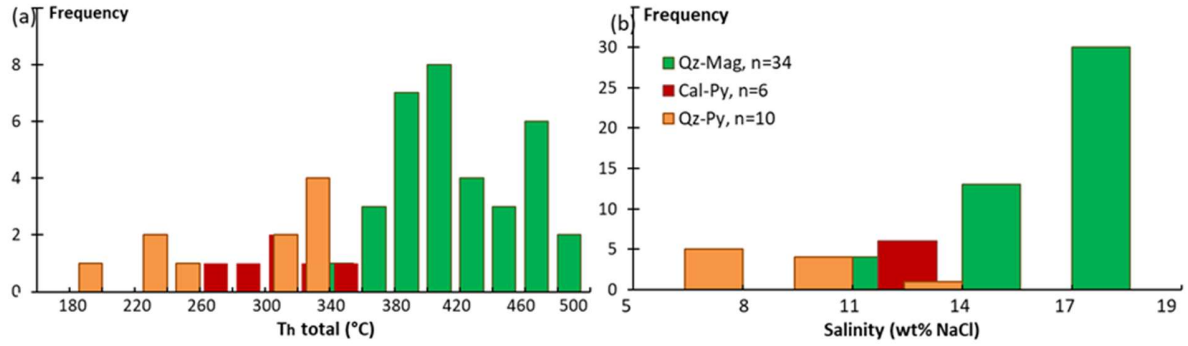

Figure 6. Microthermometry data of primary LV-type fluid inclusions hosted by quartz and calcite at the Shourab gold prospect. (a) Histograms of homogenization temperatures. (b) Histograms of salinities.

Table 3. Summary of microthermometry data of primary fluid inclusions in quartz and calcite at the Shourab gold prospect.

Stage	Host	n	FI type	Te (°C)	Tm_{ice} (°C)	Tm_{NaCl} (°C)	Salinity (wt% NaCl)	Average (wt% NaCl)	T_h (°C)	Mode (°C)
I: Qz-Mag	quartz	34	LV	-21.9 to -26	-7.5 to -15.5		11.1 to 19.1	16.7	343 to 495	390
I: Qz-Mag	quartz	1	LVS	-22	-	120	28.58	-	384	-
II: Cal-Py	calcite	6	LV	-26.6	-7.6 to -8.9		11.2 to 12.7	12.2	278 to 353	-
III: Qz-Py	quartz	10	LV	-20 to 24.5	-4.2 to -7.5		6.7 to 11.1	8.0	198 to 338	324

Key: L-liquid, S-halite, V-vapor, n= quantity of analyzed inclusions, Tm_{ice}=temperature of ice melting, Tm_{NaCl}=temperature of halite solubilization, T_h: temperature of homogenization.

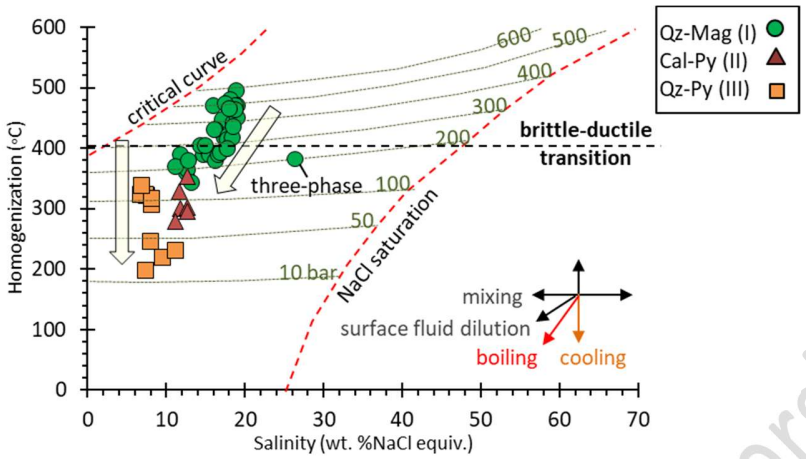

Figure 7. Plots of homogenization temperature (T_h) vs salinity (%NaCl equiv.) for Type II (LV) and III (LVS) fluid inclusions in quartz and calcite associated with magnetite and sulfide mineralization. The arrow indicates the typical fluid evolution trend (after Hezarkhani and Williams-Jones, 1998; Wilkinson, 2001). Fluid inclusion trend for stage-1 quartz show steep depletion of Salinity vs Th, steeper than the trend of fluid dilution. Green color lines represent pressure estimates for various types of fluids.

6. Discussion

6.1. Ore-forming fluid evolution and ore formation mechanism

Trace element compositions of quartz from the Shourab gold prospect provide key insights into the evolving physicochemical conditions of the mineralizing fluids. Among the analyzed elements, Al, Ti, and K are the most sensitive indicators of magmatic differentiation and their ratios (Al/Ti and Al/K) effectively track the degree of parental melt fractionation (Breiter et al. 2020). In the Shourab veins, early-stage quartz characterized by relatively low Al contents, is interpreted to have crystallized from high-temperature, near-neutral fluids. In contrast, late-stage quartz, exhibiting substantially elevated Al concentrations, formed under low tempreture, acidic conditions (Rusk et al., 2008). Potassium enrichment is attributed to coupled Al^{3+} –Si^{4+} substitution (Müller et al., 2012), whereas higher iron contents are typical of epithermal-type quartz (Table 1; Manalo et al., 2020). Titanium concentrations systematically decrease with falling precipitation temperatures, in agreement with patterns ducumented in porphyry-epithermal systems and confirmental studies (Mao et al. 2017; Acosta et al. 2020). The Al/Ti and Al/K ratios provide further discrimination between quartz populations at different stages of mineralization. Notably, late-stage quartz

displays markedly higher Al/K values, ranging from 6.2 to 17.6, while Al/Ti is below the detection limit.

Early-stage quartz from biotite-magnetite alteration contains higher Ti and lower Fe concentrations (BDL–410, Ti and 108-985 ppm Fe), suggesting formation under high-temperature (>400 °C) conditions in a magmatic-hydrothermal environment (Larsen et al., 2004; Landtwing and Pettke, 2005; Müller et al., 2010; Breiter et al, 2013). The depletion in alkali elements (Al <505 ppm, K <81 ppm) further supports a high-temperature magmatic-hydrothermal with significant influence of magmatic components. In contrast, late-stage quartz from silicified zones shows significant enrichment in Al (704–2307 ppm), Na (BDL–349 ppm), and K (96–247 ppm), along with low Ti (BDL), reflecting crystallization from lower-temperature hydrothermal fluids with increased alkali activity (Perny et al., 1992; Blankenburg et al., 1994; Wark and Watson, 2006; Jacamon and Larsen, 2009; Müller et al., 2010; Götze et al., 2021; Breiter et al., 2013; 2020; Shah et al., 2022; Keyser et al., 2023).

This shift is further supported by fluid inclusion data, which document a progressive cooling and cooling of the ore-forming fluids. Early high-temperature (~390 °C), saline fluids (11–29 wt% NaCl eq.) are recorded in LV- and LVS-type inclusions. This suggests fluid boiling (Fig. 5e), supported by various vapour/liquid ratio, that will not observe in the dilution process (Fig. 7). Microthermometric data from fluid inclusions reveals evidence of phase separation (boiling) in early-stage quartz, as indicated by variable vapor-liquid ratios and the presence of coexisting hypersaline inclusions (up to 29 wt% NaCl eq.). This process likely occurred near the brittle-ductile transition zone (~400 °C), where magmatic fluids underwent decompression (Fig. 7; Fournier, 1999). Saline, sulfur-poor fluids of this type are capable of transporting significant metal loads at elevated temperatures and tend to precipitate Fe and other nonchalcophile elements (Barton and Johnson, 1996). The subsequent carbonatization stage (stage II) records slightly lower temperatures (278 to 353 °C) and moderate salinities (11–13 wt% NaCl eq.), reflecting sustained magmatic fluid influx coupled with progressive cooling. The late silicification stage (stage III) marks a significant thermal decline (198–338 °C) and reduced salinity (6.7–11.1 wt% NaCl eq.). Under favorable redox conditions, sulfate reduction can be coupled with the oxidation of magnetite to hematite, leading to sulfide generation according to the reaction: $4H^{+}+2SO_4^{2-}+12Fe_3O_4=18Fe_2O_3+FeS_2+ 2H_2O$ (Barton, 2013).

Gold precipitation at the Shourab prospect was likely controlled by a combination of cooling and redox changes. In the earliest, high-temperature stage, magnetite was preferentially deposited, whereas pyrite-chalcopyrite mineralization developed during intermediate stages in response to increasing sulfur activity and CO_2 loss. Progressive carbonatization of the host rocks further contributed to CO_2, reinforcing these conditions. The final stage was characterized by the incursion of cooler hydrothermal fluids, which promoted gold deposition through sulfidation of earlier magnetite and/or destabilization of Au-bearing complexes (e.g., Cl^-, HS^-) as the system evolved toward temperature, higher sulfur activity and more acidic conditions (Skirrow, 2022; Song et al., 2024).

Shourab shares several characteristics with IOCG deposits, particularly in its fluid characteristics and mineralization styles. (1) Quartz chemistry reflects fluid evolution: High Ti in early quartz (BDL–410 ppm Ti) points to high temperature (>400 °C) magmatic-hydrothermal conditions, akin to porphyry/IOCG systems; (2) Fluid inclusions show cooling trends: Early saline (11–29 wt% NaCl eq.), high temperature (>400 °C) Na-K-Cl±CO_2 fluids (LV/LVS inclusions) match IOCG magmatic-hydrothermal signatures (Hitzman et al., 1992; Baker, 1998; Pollard, 2001; 2006; Sillito, 2003; Williams et al., 2011; Eslamizadeh, 2016; Fuentes-Guzmán et al., 2023; Song et al. 2024). IOCG deposits are typically formed by moderate- to high-temperature, complex brines, composed predominantly of H_2O, NaCl, and $CaCl_2$ (Hunt et al., 2007); and (3) Gold deposition was likely triggered by cooling/redox shifts: Early magnetite-hematite → intermediate pyrite-chalcopyrite (CO_2 loss, rising sulfur) → late Au via sulfidation or ligand destabilization (Cl^-/HS^-), consistent with IOCG models (Barton, 2013; Skirrow, 2022; Song et al., 2024). Strong carbonate alteration and limited potassic alteration distinguish it from typical IOCG models. These discrepancies suggest that Shourab may represent either a carbonate-rich IOCG variant or a transitional system between IOCG and other iron oxide-associated deposit types. To clarify its classification, future work should focus on detailed metal zonation patterns and geochemistry. Nevertheless, Shourab's unique attributes offer valuable insights into the diversity of iron oxide-dominated hydrothermal systems, enhancing our understanding of their genetic and alteration processes.

7. Conclusions

This study reconstructs the ore-forming fluid evolution for the Shourab gold prospect through integrated quartz chemistry and fluid inclusion analysis. The results delineate a clear physicochemical transition from early high-temperature, saline magmatic-hydrothermal fluids, that precipitated Ti-rich, alkali-poor quartz, to late-stage cooler hydrothermal fluids from which Al- and alkali-enriched (K, Na), Ti-depleted quartz crystallized. Three distinct mineralization stages are identified: (1) early high-temperature stage (>400 °C) characterized by Ti-rich quartz and high-salinity fluids (11–29 wt% NaCl eq.), (2) an intermediate transition phase marked by Fe-Mn-rich calcite precipitation at moderate temperatures (278 to 353 °C), and (3) a late, low-temperature stage (198–338 °C) hosting gold mineralization, which is associated with alkali-enriched quartz (Al 704–2307 ppm) and lower-salinity fluids (7–11 wt% NaCl eq.). This physicochemical evolution, characterized by progressive cooling, declining salinity, and increasing fluid-rock interaction, was the principal control on gold precipitation. The depositional mechanism was likely triggered by a combination of fluid cooling, dilution, and sulfidation of pre-existing magnetite, which destabilized gold complexes (e.g., Cl^-/HS^-) under increasingly acidic conditions. Calcite chemistry (FeO 0.46–1.74 wt%, MnO 0.39–2.89 wt%) confirms metal-bearing fluid circulation during carbonate alteration. This highlights the diversity within iron oxide-associated hydrothermal systems. Consequently, this study demonstrates that quartz chemistry and fluid inclusion analysis are powerful proxies for deciphering hydrothermal evolution, and it underscores the need for further research into metal zonation patterns to refine the genetic model and classification of the Shourab gold prospect.

Acknowledgements

This paper is part of the first author's Ph.D. thesis at the Islamic Azad University, Tehran, Iran. The authors would like to sincerely thank the reviewers and editors for their constructive comments and helpful suggestions, which improved the quality of the manuscript.

References

Acosta M.D., Watkins J.M., Reed M.H., Donovan J.J., DePaolo D.J. (2020) Ti in-quartz: evaluating the role of kinetics in high temperature crystal growth experiments. *Geochimica et Cosmochimica Acta* 281:149–167. https://doi.org/10.1016/j.gca.2020.04.030

Babazadeh S., Ghorbani M.R., Cottle J.M., Bröcker M. (2019) Multi-stage tectono-magmatic evolution of the central Urumieh-Dokhtar magmatic arc, south Ardestan, Iran: Insights from zircon geochronology and geochemistry. *Geological Journal* 54 (4): 2447-247. https://doi.org/10.1002 /gj.3306

Bagheri S., Stampfli G.M. (2008) The Anarak, Jandaq and Posht-e-Badam metamorphic complexes in central Iran: new geological data, relationships, and tectonic implications. *Tectonophysics* 451: 123–155. https://doi.org/10.1016/j.tecto.2007.11.047

Baker T. (1998) Alteration, mineralization, and fluid evolution at the Eloise Cu–Au deposit, Cloncurry district, NW Queensland. *Economic Geology* 93: 1213–1236. https://doi.org/10.2113/gsecongeo. 93.8.1213

Barton M.D. (2013) Iron oxide(-Cu–Au–REE–P–Ag–U–Co) systems. *Treatise on Geochemistry* 13: 515–541. https://doi.org/10.1016/b978-0-08-095975-7.01123-2

Barton M.D., Johnson D.A. (1996) Evaporitic source model for igneous-related Fe oxide–(REE–Cu–Au–U) mineralization. *Geology* 24: 259–262. https://doi.org/10.1130/0091-7613(1996)024 <0259:ESMFIR>2.3.CO;2

Blankenburg H.J., Götze J., Schulz H. (1994) Quarzrohstoffe. Deutscher Verlag für Grundstoffindustrie, Leipzig-Stuttgart, Germany, 296 pp.

Breiter K., Ackerman L., Svojtka M., Müller A. (2013) Behavior of trace elements in quartz from plutons of different geochemical signature: A case study from the Bohemian Massif, Czech Republic. *Lithos* 175–176: 54–67. https://doi.org/10.1016/j.lithos.2013.04.023

Breiter K., Ďurišová J., Dosbaba M. (2020) Chemical signature of quartz from S- and A-type rare-metal granites – A summary. *Ore Geology Reviews* 125, 103674. https://doi.org/10.1016/j.oregeorev. 2020.103674

Brown P.E., Hagemann S.G. (1994) MacFlinCor: A computer program for fluid inclusion data reduction and manipulation. In Fluid Inclusions in Minerals: Methods and Applications (de Vivo, B. & Frezzotti, M.L., eds.). Short Course IMA, VPI Press, 231-250

Brown PE, Hagemann SG (1995) MacFlinCor and its application to fluids in Archean lode-gold deposits. *Geochimica et Cosmochimica Acta* 59(19): 3943-3952. https://doi.org/10.1016/0016-7037(95)00254-w

Chiu H.Y., Chung S.L., Zarrinkoub M.H., Mohammadi S.S., Khatib M.M., Iizuka Y. (2013) Zircon U–Pb age constraints from Iran on the magmatic evolution related to Neotethyan subduction and Zagros orogeny. *Lithos* 162: 70-87. https://doi.org/10.1016/j.lithos.2013.01.006

Dabiri R., Akbari-Mogaddam M., Ghaffari M. (2018) Geochemical evolution and petrogenesis of the eocene Kashmar granitoid rocks, NE Iran: implications for fractional crystallization and crustal contamination processes, *Iranian Journal of Earth Sciences* 10 (1): 68-77.

Dennen W.H. (1966) Stoichiometric substitution in natural quartz. *Geochimica et Cosmochimica Acta* 30(12): 1235-1241. https://doi.org/10.1016/0016-7037(66)90058-5

Elmi R., Arian M. A., Ashja Ardalan A., Yazdi A. (2025) Petrology of volcanism in the Alasht-Haraz road of the Alborz mountain range, south of Amol (north of Iran), *Iranian Journal of Earth Sciences*, 17(3): 1-16. DOI: https://doi.org/10.57647/j.ijes.2025.16800

Eslamizadeh A. (2016) Geological setting of iron oxide-apatite deposits in theBafq district, central Iran with an emphasis on mineralogical, petrographic, and geochemical study of the Sechahun deposit. *Iranian Journal of Earth Sciences* 8(1): 147-163. https://oiccpress.com/ijes/article/view/5788

Farangi S., Ahmadirouhani R., Alaminia Z. (2021) Investigation of iron occurrence using Landsat 8, ASTAR and Sentinel 2 satellites remote sensing techniques in the NE Zavareh, Isfahan. The 13th national conference and the first international conference of the Economic Geology association of Iran, Lorestan university. (in Persian)

Farangi S., Alaminia Z., Vahedi M., Sadeghisorkhani H. (2023) Investigation of iron occurrence by geophysics, geochemistry, and tectonic setting of granitoids of the East of Kuh-e Dom, Central Iran. *Scientific Quarterly Journal of Geosciences* 33(2): 1-24. https://doi.org/10.22071/gsj.2023.361759.2032

Fournier R.O. (1999) Hydrothermal processes related to movement of fluid from plastic into brittle rock in the magmatic-epithermal environment. *Economic Geology* 94(8): 1193-1211.

Fuentes-Guzmán E., Camprubí A., González-Partida E., Hernández-Avilés G., Alfonso P., Cienfuegos-Alvarado E., Mesino-Hernández J.C., Ortega-Obregón C., Otero-Trujano F.J., Ramírez J.T.V. (2023) The Tatatila–Las Minas IOCG skarn (Veracruz, Mexico): Mineralogical, fluid inclusion and stable isotope constraints. *Journal of South American Earth Sciences* 122: 104112. https://doi.org/10.18268/bsgm2020v72n3a110

Gao S., Zou X., Hofstra A.H., Qin K., Marsh E.E., Bennett M.M., L.i.G., Jiang J., Su S., Zhao J., Li Z. (2022) Trace elements in quartz: Insights into source and fluid evolution in magmatic-hydrothermal systems. *Economic Geology* 117(6): 1415-1428. https://doi.org/10.5382/econgeo.4943

Götze J. (2009) Chemistry, textures and physical properties of quartz – geological interpretation and technical application. *Mineralogical Magazine* 73, 645–671. https://doi.org/10.1180/minmag.2009.073.4.645

Götze J. (2012) Mineralogy, Geochemistry and cathodoluminescence of authigenic quartz from different sedimentary rocks. pp. 287–306 in: Quartz: Deposits, Mineralogy and Analytics. (J. Götze and R. Möckel, editors). *Springer Geology*, Heidelberg-New York-Dordrecht-London. https://doi.org/10.1007/ 978-3-642-22161-3_13

Götze J., Pan Y., Müller A. (2021) Mineralogy and mineral chemistry of quartz: A review. *Mineralogical Magazine* 85(5): 639-664. https://doi.org/10.1180/mgm.2021.72

Haschke M., Ahmadian J., Murata M., McDonald I. (2010) Copper mineralization prevented by arc-root delamination during Alpine–Himalayan collision in Central Iran. *Economic Geology* 105: 855-865. https://doi.org/10.2113/gsecongeo.105.4.855

Hezarkhani A., Williams-Jones A.E. (1998) Controls of alteration and mineralization in the Sungun porphyry copper deposit, Iran; evidence from fluid inclusions and stable isotopes. *Economic Geology* 93(5): 651-670. https://doi.org/10.2113/gsecongeo.93.5.651

Hitzman MW., Oreskes N., Einaudi MT. (1992) Geological characteristics and tectonic setting of Proterozoic iron oxide (Cu- U- Au- REE) deposits. *Precambrian research* 58(1-4): 241-287. https://doi.org/10.1016/0301-9268(92)90121-4

Hunt J.A., Baker T., Thorkelson D.J. (2007) A review of iron oxide copper-gold deposits, with focus on the Wernecke Breccias, Yukon, Canada, as an example of a non-magmatic end member and implications for IOCG genesis and classification. *Exploration and Mining Geology* 16(3-4): 209-232. https://doi.org/10.2113/gsemg.16.3-4.209

Jacamon F., Larsen R.B. (2009) Trace element evolution of quartz in the charnockitic Kleivan granite, SW-Norway: The Ge/Ti ratio of quartz as an index of igneous differentiation. *Lithos* 107(3-4): 281-291. https://doi.org/10.1016/j.lithos.2008.10.016

Kananian A., Sarjoughian F., Ahmadian J. (2011) Effective Processes in Evolution of Kuh-e Dom Plutonism, NE Ardestan, the using of Geochemical and Isotopic Evidence. *Scientific Quarterly Journal of Geosciences* 21(81): 191-200. https://doi.org/10.22071/gsj.2011.54383

Kananian A., Sarjoughian F., Nadimi A., Ahmadian J., Ling W. (2014) Geochemical characteristics of the Kuh-e Dom intrusion, Urumieh–Dokhtar Magmatic Arc (Iran): Implications for source regions and magmatic evolution. *Journal of Asian Earth Sciences* 90: 137-148. https://doi.org/10.1016/j.jseaes.2014.04.026

Keyser W., Müller A., Steiner R., Erambert M., Kristoffersen M., Unterweissacher T. (2023) Alpine eclogite-facies modification of Li-Cs-Ta pegmatite from the Wolfsberg lithium deposit, Austria. *Mineralium Deposita* 58(7): 1191-1210. https://doi.org/10.1007/s00126-023-01176-w

Landtwing M., Pettke T. (2005) Relationships between SEM-cathodoluminescence response and trace-element composition of hydrothermal vein quartz. *American Mineralogist* 90: 122–131. https://doi.org/10.2138/am.2005.1548

Larsen R.B., Henderson I., Ihlen P.M., Jacamon F. (2004) Distribution and petrogenetic behaviour of trace elements in granitic pegmatite quartz from South Norway. *Contributions Mineralogy Petrology* 147: 615–628. https://doi.org/10.1007/s00410-004-0580-4

Larsen R.B., Polvé M., Juve G. (2000) Granite pegmatite quartz from Evje-Iveland: trace-element chemistry and implications for the formation of high-purity quartz. *NGU Bulletin* 436: 57–59

Manalo P.C., Subang L.L., Imai A., de los Santos M.C., Takahashi R., Blamey N.J. (2020) Geochemistry and fluid inclusions analysis of vein quartz in the multiple hydrothermal systems

of Mankayan mineral district, Philippines. *Resource Geology* 70(1): 1-27. https://doi.org/10.1111/rge.12214

Mao W, Rusk B, Yang F, Zhang M (2017) Physical and chemical evolution of the Dabaoshan porphyry Mo deposit, South China: insights from fluid inclusions, cathodoluminescence, and trace elements in quartz. *Economic Geology* 112:889–918. https://doi.org/10.2113/econgeo.112.4.889

Mazandarani R., Sheikh Zakariaee S.J., Mortazavi, S.M., Yazdi A. (In press) Geodynamics and tectonic setting of volcanic rocks from Tineh to Reineh (Haraz road) in Iran, *Geopersia*, Doi: https://doi.org/10.22059/geope.2025.395984.648823

Mehrabi B., Tale Fazel E., Tabbakh Shabani A. (2014) Whole Rock Geochemical Techniques for Discrimination of Hydrothermal Alteration of the Kuh-e Dom Fe-Cu (±Au) prospect, Central Iran. *Advanced Applied Geology* 4(1): 58-74

Mollai H., Dabiri R., Torshizian H. A., Pe-Piper G., Wang W. E. (2021) Upper Neoproterozoic garnet-bearing granites in the Zeber-Kuh region from east central Iran micro plate: Implications for the magmatic evolution in the northern margin of Gondwanaland, *Geologica Carpathica* 72 (6): 461-81. DOI: https://doi.org/10.31577/GeolCarp.72.6.2

Müller A., Herrington R., Armstrong R., Seltmann R., Kirwin D.J., Stenina N.G., Kronz A. (2010) Trace elements and cathodoluminescence of quartz in stockwork veins of Mongolian porphyry-style deposits. *Mineralium Deposita* 45: 707–727. https://doi.org/10.1007/s00126-010-0302-y

Müller A., Wanvik J.E., Ihlen P.M. (2012) Petrological and chemical characterisation of high-purity quartz deposits with examples from Norway. Pp. 71–118 in: Quartz: Deposits, *Mineralogy and Analytics*. (J. Götze and R. Möckel, editors). Springer Geology, HeidelbergNew York-Dordrecht-London. https://doi.org/10.1007/978-3-642-22161-3_4

Perny B., Eberhardt P., Ramseyer K., Mullis J. (1992) Microdistribution of aluminium, lithium and sodium in quartz: Possible causes and correlation with short-lived cathodoluminescence. *American Mineralogist* 77: 534–544

Pollard P.J. (2001) Sodic (–calcic) alteration in Fe-oxide–Cu–Au districts: an origin via unmixing of magmatic H_2O–CO_2–NaCl±$CaCl_2$–KCl fluids. *Mineralium Deposita* 36: 93-100. https://doi.org/10.1007/s001260050289

Pollard P.J. (2006) An intrusion-related origin for Cu–Au mineralization in iron oxide–copper–gold (IOCG) provinces. *Mineralium Deposita* 41: 179-187. https://doi.org/10.1007/s00126-006-0054-x.

Roedder E. (1984) Volume 12: fluid inclusions. Rev. *Minerals* 12, p.644. https://doi.org/10.1515/9781501508271

Romanko E., Kokorin YU., Krivyakin B., Susov M., Morozov L., Sharkovski M. (1984) Outline of metallogeny of Anarak area (Central Iran): Technoexport. Report. TE/No. 19, 143 p.

Rottier B., Casanova V. (2021) Trace element composition of quartz from porphyry systems: A tracer of the mineralizing fluid evolution. *Mineralium Deposita* 56(5): 843-862. https://doi.org/10.1007/s00126-020-01009-0

Rusk B. (2012) Cathodoluminescent textures and trace elements in hydrothermal quartz. In Quartz: Deposits, mineralogy and analytics (p: 307-329). Berlin, Heidelberg: Springer Berlin Heidelberg. https://doi.org/10.1007/978-3-642-22161-3_14

Rusk B., Koenig A., Lowers H. (2011) Visualizing trace element distribution in quartz using cathodoluminescence, electron microprobe, and laser ablation-inductively coupled plasma-mass spectrometry. *American Mineralogist* 96(5-6): 703-708. https://doi.org/10.2138/am.2011.3701

Rusk B., Reed M. (2002) Scanning electron microscope–cathodoluminescence analysis of quartz reveals complex growth histories in veins from the Butte porphyry copper deposit, Montana. *Geology* 30(8): 727-730. https://doi.org/10.1130/0091-7613(2002)030%3C0727:semcao%3E2.0.co;2

Rusk B.G., Lowers H.A., Reed M.H. (2008) Trace elements in hydrothermal quartz: Relationships to cathodoluminescent textures and insights into vein formation. *Geology* 36(7): 547-550. https://doi.org/10.1130/g24580a.1

Sarjoughian F., Kananian A., Ahmadian J. (2012) Application of pyroxene chemistry for evaluation of temperature and pressure in the Kuh-e Dom intrusion, *Petrological Journal* 3(11): 97-110.

Sarjoughian F., Kananian A., Ahmadian J. (2014) Compositional Zoning in Feldspars of the Kuh-e Dom Intrusive Rocks. *Scientific Quarterly Journal of Geosciences* 24(93): 133-146. https://doi.org/10.22071/gsj.2014.43554

Sarjoughian F., Kananian A., Ahmadian J., Murata M. (2015a) Chemical composition of biotite from the Kuh-e Dom pluton, Central Iran: implication for granitoid magmatism and related Cu–Au mineralization. *Arabian Journal of Geosciences* 8: 1521-1533. https://doi.org/10.1007/s12517-013-1242-5

Sarjoughian F., Kananian A., Esna-Ashari A., Ahmadian J. (2015b) U-Pb Zircon Dating of Kuh-e Dom Intrusion, its Dikes and Enclaves. *Scientific Quarterly Journal of Geosciences* 24(95): 145-154. doi: 10.22071/gsj.2015.42422

Shah S.A, Shao Y., Zhang Y., Zhao H., Zhao L. (2022) Texture and trace element geochemistry of quartz: a review. *Minerals* 12(8): 1042. https://doi.org/10.3390/min12081042

Shahzeydi M., Moayyed M., Moazzen M., Ahmadian J. (2008) Minaralogy, thermobarometery and magmatic series of volcanic rocks in Kuh-e Dom, Ardestan. *Iranian Journal of Crystallograohy and Mineralogy* 16(3): 485-504. (In Persian). http://ijcm.ir/article-1-630-fa.html

Sharkovski M., Filichev I., Selivanov E. (1981) Geological map of Kuh-e Dom, scale 1:100000. Geological Survey of Iran.

Sillitoe R.H. (2003) Iron oxide-copper-gold deposits: an Andean view. *Mineralium Deposita* 38: 787-812. https://doi.org/10.1007/s00126-003-0379-7

Skirrow R.G. (2022) Iron oxide copper-gold (IOCG) deposits–A review (part 1): Settings, mineralogy, ore geochemistry and classification. *Ore Geology Reviews* 140: 104569. https://doi.org/10.1016/j.oregeorev.2021.104569

Song M., Peng Y., Chen Y., Zhang Y., Yang H., Xu S. (2024) Research progress of fluid inclusions and its application in iron oxide copper-gold (IOCG) deposits. *Ore and Energy Resource Geology*: 100066. https://doi.org/10.1016/j.oreoa.2024.100066

Tale Fazel E. (2014) The tectonomagmatic setting and ore-forming fluid composition of Kuh-e Dom Fe(±Cu-Au-Bi-Ag) prospect, Anarak metallogenic complex. PhD thesis in Kharazmi university of Tehran. (in Persian)

Tale Fazel E., Mehrabi B., Tabbakh Shabani A.A. (2015) Kuh-e Dom Fe–Cu–Au prospect, Anarak metallogenic complex, Central Iran: a geological, mineralogical and fluid inclusion study. *Mineralogy and Petrology* 109(1): 115-141, https://doi.org/10.1007/s00710-014-0354-2

Talebian Borojenie H, Sheykhzakariaei S.J., Dabiri R., Yazdi A. (2025) Petrogenesis and tectonic implications of Neoproterozoic to Cenozoic A-type granitoids in NW Iran: geochemical and tectonic constraints, *Iranian Journal of Earth Sciences*, 17(4): 1-19. DOI: https://doi.org/10.57647/j.ijes.2025.16894

Wark D.A., Watson E.B. (2006) TitaniQ: a titanium-in-quartz geothermometer. *Contributions to Mineralogy and Petrology* 152(6): 743-754. https://doi.org/10.1007/s00410-006-0132-1

Wertich V., Leichmann J., Dosbaba M., Götze J. (2018) Multi-stage evolution of gold-bearing hydrothermal quartz veins at the Mokrsko gold deposit (Czech Republic) based on cathodoluminescence, spectroscopic, and trace elements analyses. *Minerals* 8(8): 335. https://doi.org/10.3390/min8080335

Wilkinson J.J. (2001) Fluid inclusions in hydrothermal ore deposits. *Lithos* 55(1-4): 229-272. https://doi.org/10.1016/s0024-4937(00)00047-5

Williams M.R., Holwell D.A., Lilly R.M., Case G.N., McDonald I. (2011) Mineralogical and fluid characteristics of the fluorite-rich Monakoff and E1 Cu–Au deposits, Cloncurry region, Queensland, Australia: Implications for regional F–Ba-rich IOCG mineralisation. *Ore Geology Reviews* 64: 103-127. https://doi.org/10.1016/j.oregeorev.2014.05.021

Zhou H., Müller A., Berndt J. (2023) Quartz chemistry fingerprints melt evolution and metamorphic modifications in high-purity quartz deposits. *Geochimica et Cosmochimica Acta* 356: 179-195. https://doi.org/10.1016/j.gca.2023.07.015